Materialia 26 (2022) 101557

Contents lists available at ScienceDirect

Materialia

journal homepage: www.elsevier.com/locate/mtla

Full Length Article

Tailoring thermal and chemical properties of a multi-component environmental barrier coating candidate $(Sc_{0.2}Nd_{0.2}Er_{0.2}Yb_{0.2}Lu_{0.2})_2Si_2O_7$

Mackenzie J. Ridley*, Kathleen Q. Tomko, John A. Tomko, Eric R. Hoglund, James M. Howe, Patrick E. Hopkins, Elizabeth J. Opila

Materials Science and Engineering, University of Virginia, USA

ARTICLE INFO

Keywords:
Environmental barrier coating
Phase stability
CMAS
Thermal conductivity

ABSTRACT

Environmental barrier coatings, typically rare earth silicates, have been successfully employed on ceramic matrix composites in the hot zone of gas turbine engines, allowing for high fuel burn temperatures and increased flight efficiency. Yet, environmental barrier coatings face challenges as turbine temperatures continue to increase, such as increased oxidation of the underlying substrate, environmental degradation, and coating spallation. Here, we show how multi-component rare earth silicates offer a unique solution for simultaneously co-optimizing phase stability, thermo-chemical, and thermo-mechanical properties through variation of the rare earth elements implemented in the coating material. Each rare earth element added in solution was chosen to enhance specific material properties. We found that chemical stability with the turbine gaseous environment or with molten deposits could be retained, and in some cases enhanced, without detrimental effects on the phase stability or thermo-mechanical behavior. Our results demonstrate how rare earth cation mixing can lead to a 50% reduction in thermal conductivity for the given rare earth silicate mixtures. Such decreases in thermal conductivity show promise for reducing the substrate operating temperature during use, thus making multi-component rare earth silicates a novel class of dual-purpose thermal/environmental barrier coating materials.

1. Introduction

Environmental Barrier Coatings (EBCs) are a required technology for application of SiC_{fiber}/SiC_{matrix} ceramic matrix composites (CMCs) in the hot section of airplane turbines. EBCs mitigate interaction between the combustion environment and the CMC to prevent a wide variety of known failure modes: CMC oxidation, volatilization from high-temperature steam reactions, and reaction with CaO-MgO-Al_2O_3-SiO_2 (CMAS) molten deposits. EBC material candidates are most often silicates to maintain chemical compatibility with the SiC CMC and must also match the coefficient of thermal expansion (CTE) of the CMC to limit stress buildup upon thermal cycling. It is hypothesized that the state-of-the-art EBC, $Yb_2Si_2O_7$ (YbDS), can be improved by introducing multiple rare earth cations in a solid solution, where each additional rare earth can be used to mitigate a specific degradation process and simultaneously lower the thermal conductivity. This work explores a novel rare earth disilicate, $(Sc_{0.2}Nd_{0.2}Er_{0.2}Yb_{0.2}Lu_{0.2})$DS, to determine the efficacy of multi-component silicates for tailoring properties of EBCs for application in combustion environments.

Combustion environments can result in material temperatures of 1100–1400 °C [1–3], gas velocities of 100–668 m/s [2,3], 6–31 atm total pressure [2] and a 10% water vapor atmosphere [4], such that steam reaction will occur consistently throughout EBC lifetime. Rare earth silicate EBCs are known to react with water vapor by volatilizing the SiO_2 component as $Si(OH)_4$ (g) [5]. Recently, a variety of reactions have been experimentally determined or predicted for various rare earth disilicates.

$$RE_2Si_2O_7 + 2H_2O(g) \rightarrow RE_2SiO_5 + Si(OH)_4(g) + porosity \quad (1)$$

$$14RE_2Si_2O_7 + 20H_2O(g) \rightarrow 3RE_{9.33}\square_{0.67}Si_6O_{26} + 10Si(OH)_4(g) + porosity \quad (2)$$

$$RE_2Si_2O_7 + 4H_2O(g) \rightarrow RE_2O_3 + 2Si(OH)_4(g) + porosity \quad (3)$$

Eq. (1) represents the most common steam reaction for $RE_2Si_2O_7$ (REDS), and is reported for RE = Er, Yb, Y, and Lu [6–10]. A notional steam reaction for rare earth apatite formation, shown in Eq. (2), is consistent with experimental observation of the reaction product formed on NdDS after high-velocity steam exposure, where □ in Eq. (2) represents vacancies on the rare earth site [6]. Eq. (3) has been observed for ScDS, which directly formed Sc_2O_3 after steam exposure, suggesting instability

* Corresponding author.
E-mail address: ridleymj@ornl.gov (M.J. Ridley).

https://doi.org/10.1016/j.mtla.2022.101557
Received 1 July 2022; Accepted 27 August 2022
Available online 28 August 2022

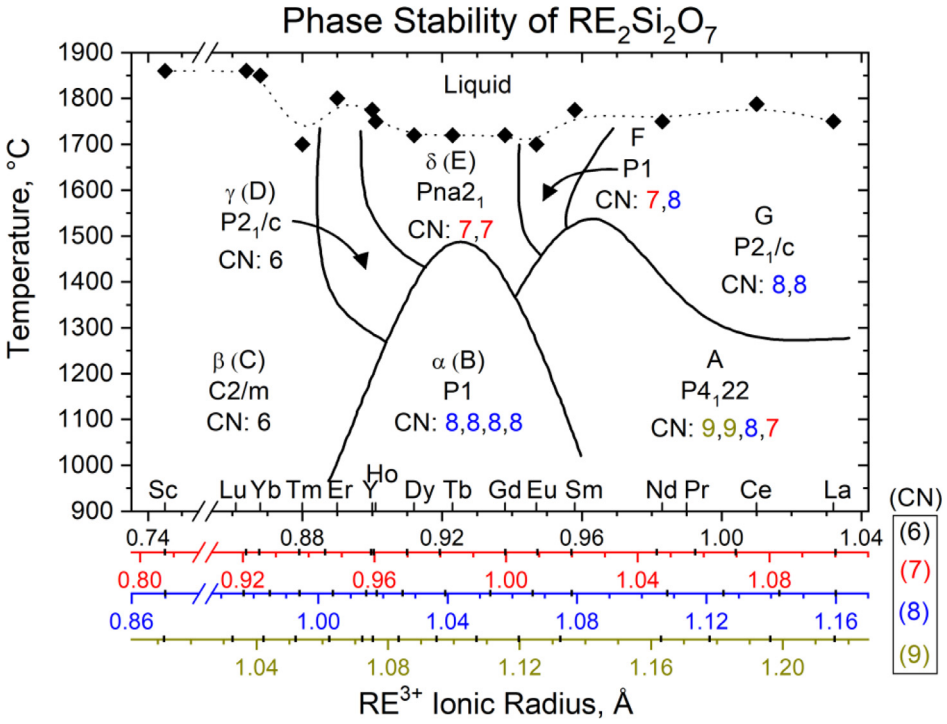

Fig. 1. Polymorph stabilities of rare earth disilicates, adapted from Turcer and Padture [22] to include polymorph/phase identification, space groups, RE – O coordination numbers (CN), and melting temperatures. Each RE – O coordination number has its own associated x-axis for ionic radius, which are color coded.

of Sc_2SiO_5 [6]. All of the listed reactions produce a volatile gas species, resulting in formation of porosity in the solid product phase.

Dust, sand, and fly ash can enter the engine during flight and become molten in the turbine hot section with a nominal composition of $CaO{\cdot}MgO{\cdot}AlO_{1.5}{\cdot}SiO_2$ (CMAS). The molten deposits on the EBC surface result in glass infiltration, chemical reactions, and EBC dissolution into the melt [11,12]. Formation of a continuous reaction product between the CMAS and the outer EBC layer can be used to limit further CMAS melt infiltration [13–16]. Generalized reactions between CMAS and rare earth silicates are presented in Eqs. (4) and (5) for the formation of the primary reaction product, calcium-rare earth apatite [17].

$$4RE_2SiO_5 + 2CaO + 2SiO_2 \rightarrow Ca_2RE_8(SiO_4)_6O_2 \quad (4)$$

$$4RE_2Si_2O_7 + 2CaO \rightarrow Ca_2RE_8(SiO_4)_6O_2 + 2SiO_2 \quad (5)$$

$Ca_2RE_8(SiO_4)_6O_2$ contains two unique rare earth sites, which typically results in Ca and RE both occupying the ninefold coordinated site, and RE occupying the sevenfold coordination site [18]. CMAS deposition is likely to occur on the porous steam reaction product of an EBC, suggesting CMAS reaction studies should be performed on silica-depleted materials such as RE_2SiO_5 (REMS) or RE_2O_3. It has been shown that YbMS more rapidly reacts with CMAS to form a dense apatite layer compared to a detrimental CMAS infiltration reaction with YbDS [17,19]. Multicomponent REDS could result in EBCs with increased chemical performance due to conflicting trends in the desired EBC thermochemical properties with rare earth cation size and mass. For example, stability against molten CMAS attack increases with *increasing* the rare earth cation size [20,21], while the stability against steam attack increases with decreasing rare earth cation size [6].

A wide variety of stable structures and polymorph transitions are present for the rare earth disilicates at the operating temperatures of turbines (1000–1500 °C), as shown on the stability plot in Fig. 1 [22]. Each polymorph has its own associated rare earth cation coordination numbers (CN) and crystal structure. The β- and γ- phases generally show the best thermal expansion matches with SiC [22]. Polymorph transitions must be avoided to minimize internal stress buildup and coating spallation from thermal cycling and to limit changes in CTE, and variations in polymorph properties such as CTE or melting temperature between each REDS should be considered when mixing. REMS are stable as only two polymorphs, typically termed the X1 (RE = La – Tb, Y) and X2 (RE = Tb – Lu, Y, Sc) phases [23].

Table 1
Rare earth assemblage based on rare earth (RE) REDS properties.

	REDS				
	Sc	Nd	Er	Yb	Lu
β-Phase Stability	✔			✔	✔
Steam Resistance			✔	✔	✔
CMAS Resistance		✔			
Decreased Thermal Conductivity	✔	✔			

Phase stability and CTE requirements have limited EBC candidates to the smaller ionic radius β-phase REDS, yet multicomponent silicates can allow for the introduction of larger rare earth cations to the low-CTE β-phase. For example, Yb additions to YDS to produce $(Y_{0.6}Yb_{0.4})$DS has been utilized to stabilize the β-phase for yttrium silicates [24], which also resulted in enhanced oxidation resistance compared to YbDS/YbMS EBCs [25,26]. $(Yb_{0.2}Y_{0.2}Lu_{0.2}Sc_{0.2}Gd_{0.2})$DS is stable as a low CTE β-phase while YDS and GdDS are not [27]. Similarly, the high-temperature γ-phase for ErDS was avoided through phase stabilization in a β-phase $(Er_{0.25}Tm_{0.25}Yb_{0.25}Lu_{0.25})$DS [28]. Multi-component ceramics have also shown dramatic reductions (25-80%) in thermal conductivity through mass scattering at the crystal lattice [29–32]. Multicomponent REDS thus show promise as dual-purpose thermal/environmental barrier coating (T/EBC) materials, where a lower CMC surface temperature could decrease the oxidation rate at the CMC/EBC interfaces.

Based on available data in experimental literature, the rare earth assemblage of Sc, Nd, Er, Yb, and Lu was chosen to demonstrate the potential to co-optimize desired rare earth silicate EBC properties, where the rationale as follows is summarized in Table 1: Sc, Yb, and Lu are expected to stabilize the β phase [23]; Er, Yb, and Lu are expected to enhance steam resistance [6]; Nd is expected to enhance CMAS resistance [20,21]; Sc and Nd are expected to lower thermal conductivity [29,30]. $(Sc_{0.2}Nd_{0.2}Er_{0.2}Yb_{0.2}Lu_{0.2})_2Si_2O_7$, termed (ScNdErYbLu)DS throughout

Table 2
Characterization of starting materials.

Material	Density (g/cm^3)	Porosity (%)	Phase Composition
(ScNdErYbLu)DS	5.27 ± 0.02	4	~93% β: (ScNdErYbLu)DS, ~7% G: (ScNdErYbLu)DS
(ScNdErYbLu)MS	5.94 ± 0.03	11	100% (ScNdErYbLu)MS

the rest of this work, was exposed to high-velocity steam for 125 h at 1400 ˚C to determine the reaction products, phase stability, and microstructural changes. Bulk $(Sc_{0.2}Nd_{0.2}Er_{0.2}Yb_{0.2}Lu_{0.2})_2SiO_5$ material, now referred to as (ScNdErYbLu)MS, was then prepared to represent the porous steam reaction product and was exposed to CMAS at 1300 ˚C for 24 h. Thermal expansion (dilatometry) and thermal conductivity (time-domain thermoreflectance) were measured for each (ScNdErYbLu) silicate compound and compared to YbDS and YbMS.

2. Methods

2.1. Processing

High purity pre-reacted silicate powders (Praxair Surface Technologies, Danbury, CT) were used for processing of both silicate materials. Equimolar powder ratios were ball milled for 24 h prior to consolidation. (ScNdErYbLu)DS powder was heated in air at 900 ˚C for 30 min, loaded into a 20 mm diameter graphite die, and then sintered with spark plasma sintering (SPS: Thermal Technologies DCS 25-10 SPS, Santa Rosa, CA) at 1525 ˚C and 65 MPa in argon for 1 h with a 125 ˚C/min heating rate and 30 ˚C/min cooling rate. The sintered sample was placed on platinum foil and heated in a lab air alumina box furnace (CM Rapid Furnace, Bloomsfield, NJ) for 24 h at 1500 ˚C to restore oxygen stoichiometry and remove residual carbon. Due to the known anisotropic nature of REMS [29], pressureless sintering method was used to densify (ScNdErYbLu)MS to mitigate specimen microcracking. After ball milling, two grams of (ScNdErYbLu)MS powder mixture was combined with four drops of polyvinyl alcohol solution and pressed in a 0.5-inch diameter steel die to 80 MPa. The green body was placed on platinum foil and sintered in a box furnace at 1600 ˚C for 32 h with 10 ˚C/min heating and cooling rates.

Results of initial characterization of each material are presented in Table 2. Densities of both (ScNdErYbLu) silicates were measured five times via Archimedes method in deionized water and averaged. The measured density of (ScNdErYbLu)DS was 5.27 ± 0.02 g/cm^3 after processing, compared to a theoretical rule of mixtures density of 5.37 g/cm^3. (ScNdErYbLu)DS showed 4% porosity by SEM image area fraction. (ScNdErYbLu)MS had an averaged density of 5.94 ± 0.03 g/cm^3 with ~11% porosity by image area fraction, compared to a theoretical rule of mixtures density of 6.23 g/cm^3. (ScNdErYbLu)DS was multi-phase, where less than 7% of the G-REDS phase was estimated from comparison of maximum XRD peak intensities for the β- and G-REDS phases. Any impurity phase was below the detectable limit by XRD for (ScNdErYbLu)MS, where all peaks matched the X2 phase REMS. XRD data will be presented later in the results section.

2.2. High-velocity steam reactivity

High-velocity steam testing was performed on (ScNdErYbLu)DS with a modified tube furnace experimental setup, termed a steamjet, which has been described in detail elsewhere [33–35]. The steamjet achieved gas velocities up to 240 m/s, representative of a turbine environment, and operates at 1 atm total pressure and 1 atm H_2O (g). The (ScNdErYbLu)DS sample was oriented 45˚ relative to the capillary outlet such that high-velocity steam impinged in the center of the sample and then flowed to one side of the sample. Each test sample had a high velocity impingement site and a large steam velocity gradient across the rest of the surface. Steam velocities were calculated with ANSYS (Canonsburg, PA) computational fluid dynamics [36]. The steam velocity at the impingement site was found to be near 240 m/s for a measured liquid water flow rate of 1.95 ± 0.05 ml/min.

X-ray diffraction (XRD: PANalytical Empyrean Diffractometer, Westborough, MA) and scanning electron microscopy (SEM: FEI Quanta 650, Hillsboro, OR) was performed in plan view on the sample before and after steam exposure. The sample was then mounted and polished in cross-section through the highest velocity impingement site. Steam reaction depths were measured with ImageJ analysis suite (National Institutes of Health, Bethesda, Maryland) every 62 μm across the sample.

Cross sectional samples of (ScNdErYbLu)DS after exposure to high velocity steam were prepared for scanning transmission electron microscopy (STEM) using a Thermo Fisher Helios dual-beam focused ion-beam (Waltham, MA). Energy dispersive X-ray spectroscopy (EDS) was used to characterize phases present, site segregation, and reaction mechanism. Monochromated electron energy-loss spectroscopy (EELS) was then used to provide an understanding of bonding within the various phases. Beam currents of 400 pA and 150 pA were used for EDS and EELS, respectively. EELS acquisition was performed with an energy-resolution of 0.16 eV (measured as the zero-loss full-width at half-maximum) and captured using a Gatan Imaging Filter (GIF) equipped with a K2 camera. Additional TEM characterization and results can be found in Supplementary Materials.

2.3. CaO-MgO-Al_2O_3-SiO_2 reactivity

(ScNdErYbLu)MS was exposed to 41.5 mg/cm^2 loading of CMAS with a composition 33CaO-9MgO-13$AlO_{1.5}$-45SiO_2, which had a melting temperature near 1235 ˚C [17,37]. A high CMAS loading was chosen in this study to better visualize the reaction products and is not representative of the typical CMAS exposure in the field. CMAS was prepared from mixing the respective oxides in a high-purity platinum crucible at 1300 ˚C for 24 h. The resulting glass was quenched and crushed into a powder. Green body CMAS pellets were prepared at 20 MPa uniaxial pressure for three minutes, followed by sintering at 1200 ˚C for 4 h. The sintered CMAS pellet was placed on top of the 1200 grit polished sample and exposed at 1300 ˚C for 24 h in air with 10 ˚C/min heating and cooling rates.

The CMAS pellet and (ScNdErYbLu)MS combined mass were recorded before and after exposure to an accuracy of 0.05 mg (MS105DU, Mettler-Toledo, Columbus, OH). XRD was performed in plan view after exposure. SEM and EDS (Oxford Instruments, Abingdon, UK) analysis were performed in cross-section with a 15 kV accelerating voltage and 4.5 spot size at a working distance of 10 mm. Point EDS of the apatite reaction product at the interface was measured five times and averaged. Due to the unreliability of oxygen concentrations measured via EDS, cation ratios were used to determine compositions of the phases present. A metric for CMAS resistance is the material's ability to quickly form a continuous and dense interfacial reaction product that inhibits further CMAS penetration in the bulk of the material. ImageJ was used to determine the average reaction product thickness across 9.55 mm of the sample cross-section with measurements of the reaction product thickness taken every 83 μm. The amount of REMS dissolution into CMAS was measured every 313 μm using the unreacted sample edges as reference to the initial sample height.

2.4. Thermal expansion and thermal conductivity measurements

Thermal expansion was measured three times and averaged up to 1250 ˚C in air with a dilatometer (Netzsch DIL402c, Burlington, MA)

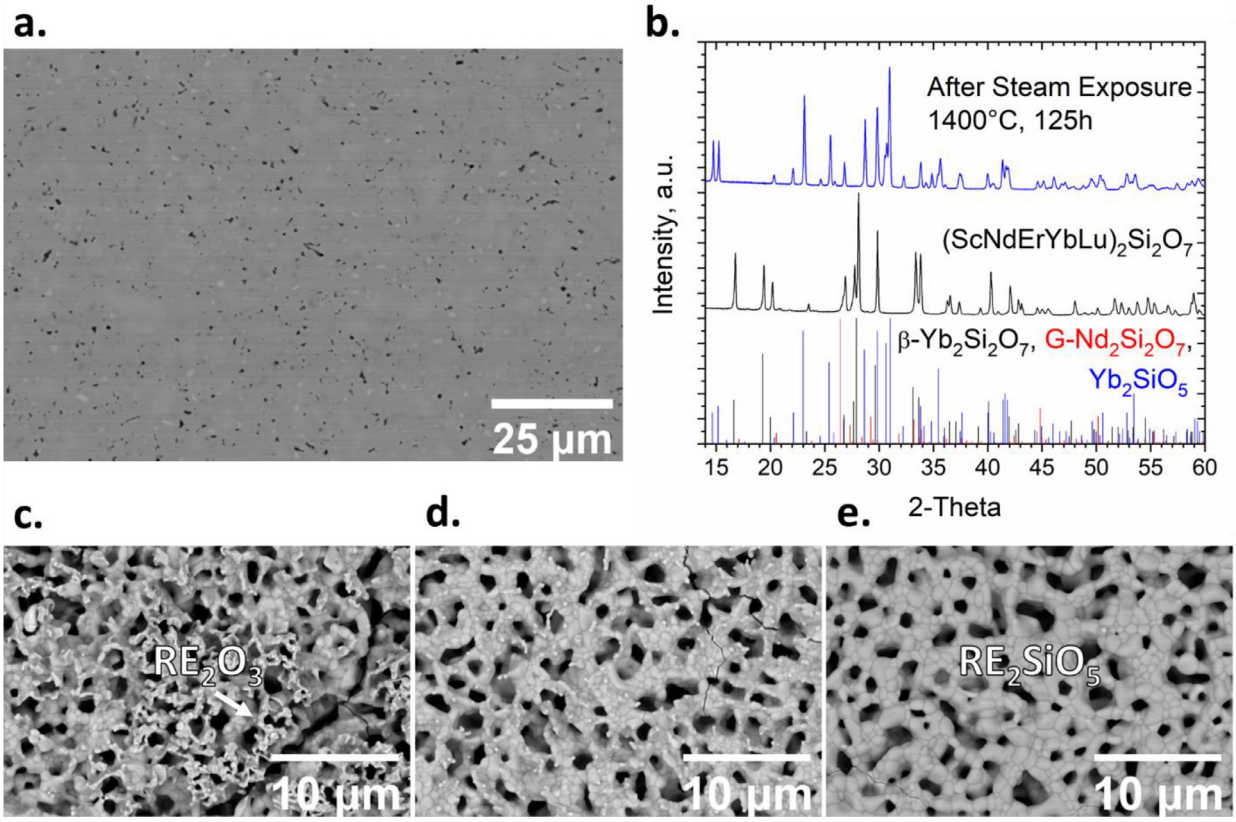

Fig. 2. a. SEM image of a multi-phase (ScNdErYbLu)DS after processing, b. X-ray diffraction before and after exposure to high-velocity steam at 1400 °C for 125 h, and (c–e) plan view SEM of (ScNdErYbLu)DS after steam exposure showing c. sparse RE_2O_3 formation at 1 mm downstream (190–200 m/s), d. RE_2SiO_5 formation at 3 mm downstream (110–130 m/s), and e. REMS formation at 6 mm downstream (70–80 m/s).

at 10 °C/min under an applied load of 30 cN. Room temperature thermal conductivity was measured by the time domain thermoreflectance (TDTR) method [38–40] with an 80 nm thick aluminum thin film transducer. TDTR is a laser-based pump-probe technique, where the sample experiences localized heating events induced by a high energy pump laser and a laser probe monitors the transient cooling of these heating events via changes in reflectivity (i.e., the probe measures the thermoreflectance of the sample). The measured 'cooling curve' was fit with a multi-layer heat diffusion equation using a least-squares minimization approach [41]; the sample thermal conductivity and the thermal boundary resistance associated with the metal transducer/sample interface were the free variables of the fitting procedure. For TDTR experiments, the laser probe had a diameter of approximately 10 μm, allowing for determination of intrinsic thermal conductivity without impact from cracks or porosity. The reported thermal conductivity measurements are the average of five positions across the center of each sample.

3. Results

3.1. (ScNdErYbLu)DS and steamjet exposure

A backscattered electron image of the starting two-phase (ScNdErYbLu)DS and X-ray diffraction (XRD) spectra before and after steam exposure at 1400 °C for 125 h are shown in Fig. 2a and b. Reference patterns for β-phase YbDS and G-phase NdDS were matched to the starting material, representative of the two phases present. All XRD peaks corresponded to the X2-phase YbMS as the solid solution reaction product after steam exposure. The detrimental steam reaction products that have been observed for phase pure ScDS and NdDS Eqs. (2) and ((3)) [6] were avoided through the presence of RE = Er, Yb, and Lu rare earth elements in the two-phase material. Backscattered electron images of the (ScNdErYbLu)DS surface after steam exposure are displayed in Fig. 2(c–e) for three local steam velocity regions: a. 190–200 m/s, b. 110–130 m/s, and c. 70–80 m/s. A porous REMS product layer was formed after steam exposure in all three velocity regions. A second reaction product, RE_2O_3, was observed on the REMS layer in Fig. 2d as small nodules. Fig. 2c shows a nonuniform and scattered layer of RE_2O_3 consistent with Reaction 4, suggesting the REMS was fairly resistant to further steam reaction at all velocity regimes of this work.

Elemental mapping for the (ScNdErYbLu)DS cross-section after steam reaction is shown in Fig. 3. The multi-phase nature of the starting material can be immediately visualized in the Nd map, consistent with the presence of a Nd-rich G-phase REDS. In agreement with XRD results, the porous product phase was depleted in SiO_2 with an EDS composition consistent with REMS. The dispersion of rare earth elements within the porous REMS product phase was uniform, suggesting elevated solubility of Nd in the X2-REMS structure compared the β-REDS structure at 1400 °C. NdMS is only thermodynamically stable as an X1-phase REMS. The steam reaction product showed that NdMS can be stabilized as the X2-phase through formation of a (ScNdErYbLu)MS solid solution.

As steam velocities increase to the 150–200 m/s range, the reaction layer thickness decreased. Coarsening behavior of a steam reaction product at elevated gas velocities has been observed for rare earth disilicates (REDS: RE = Nd, Y, Er, Yb, and Lu) exposed in the steamjet under the same conditions, which also resulted in decreased total reaction depths [6,9,35]. Such coarsening may inhibit gas transport to the interface, resulting in decreased steam reactivity with time as was seen with (ScNdErYbLu)DS. Comparison of the material in this study to that of YbDS is presented on Table 3 . Despite similar reaction depth values, YbDS from previous work formed a continuous Yb_2O_3 secondary reaction product

Table 3
Reaction depth analysis of (ScNdErYbLu)DS after steam exposure for 125 h at 1400 °C. Three velocity regimes are compared to results for YbDS [9].

REDS, RE	Average Reaction Depth, μm (m/s)	Average Reaction Depth, μm (m/s)	Impingement Depth, μm (m/s)
(ScNdErYbLu)	46 ± 3 (60–125 m/s)	28 ± 8 (125–200 m/s)	31 ± 12 (200–235 m/s)
Yb	51 ± 2 (80–115 m/s)	22 ± 3 (150–200 m/s)	37 ± 6 (200–235 m/s)

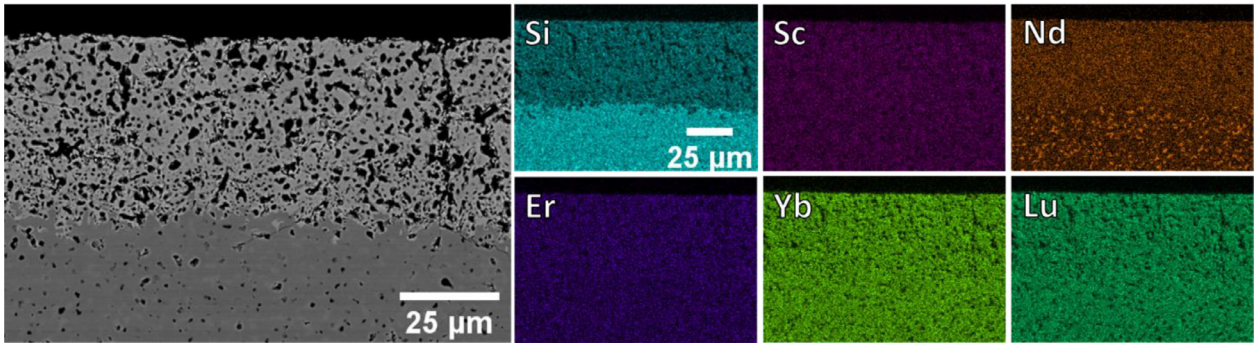

Fig. 3. SEM cross-section of (ScNdErYbLu)DS after steam exposure with EDS mapping of the reaction interface.

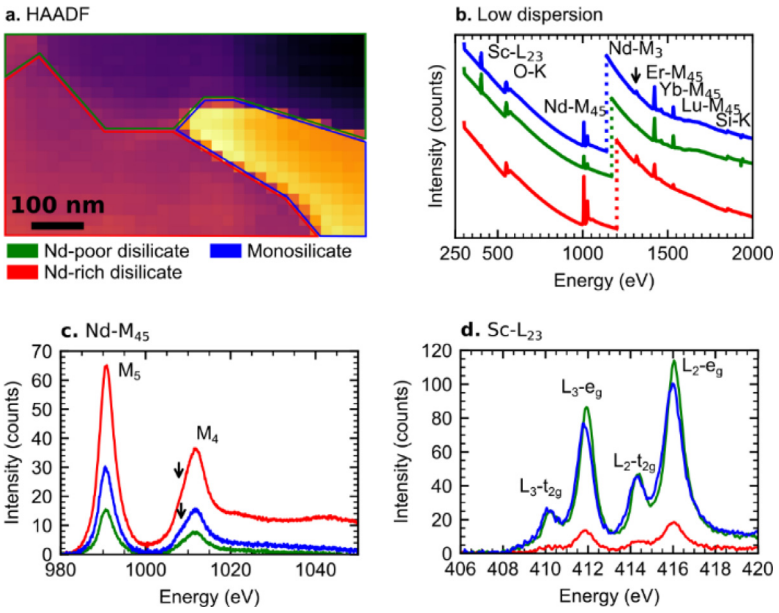

Fig. 4. EELS analysis of (ScNdErYbLu)DS interface after steam reaction at 1400 °C for 125 h. Arrows indicate the Nd-M_3 peak in (b) and a Nd satellite peak in (c).

outer layer in the high velocity (150–200 m/s) regime [9], while (ScNdErYbLu)DS in this study had negligible rare earth oxide formation on the surface. Thus, (ScNdErYbLu)MS appears to have increased resistance to steam reaction compared to pure YbMS. The stability of the dual phase (ScNdErYbLu)DS also suggests that multi-component EBCs are not limited to single phase solid solution materials if phase transformations are avoided within the temperature range of gas turbine engines.

Monochromated EELS was used to examine the near-edge structure of the (ScNdErYbLu)DS interface after steam reaction to further understand the site occupancy and preferential segregation of RE elements. Fig. 4(a) shows a HAADF image taken at a triple point between the β-REDS (green), Nd-rich G-REDS (red), and the REMS (blue), and Fig. 4(b) shows the energy spectrum for each phase. Monochromated EELS spectrum images of Nd-M_{45} and Sc-L_{23} are also shown in Fig. 4(c) and Fig. 4(d). Segregation of Sc and Nd cations is present between the disilicate phases, while all elements uniformly mix in the monosilicate phase. Further analysis on site preference can be found in Supplementary Materials.

Rare earth cations Sc, Er, Yb, and Lu all intermix in the β-phase REDS. A secondary phase in (ScNdErYbLu)DS was determined to be Nd-rich G-phase REDS. The G-phase is the high-temperature polymorph of NdDS, whereas the A-polymorph was expected from the phase diagram, signifying phase stabilization through introduction of multiple rare earth cations. A high concentration of Er was found in the Nd-rich phase, presumably due to similar ionic radii and space groups ($P2_1/c$) for the γ-ErDS and G-NdDS high-temperature polymorphs.

3.2. (ScNdErYbLu)MS and CMAS exposure

Fig. 5 displays the starting (ScNdErYbLu)MS microstructure in plan view, where the sample appeared to be mostly single phase with around 11% porosity by image area fraction.

XRD spectra of the (ScNdErYbLu)MS surface before and after 41.5 mg/cm^2 of CMAS exposure at 1300 °C for 24 h are shown in Fig. 6. The base material peaks correspond only to the X2-phase Yb_2SiO_5. XRD peaks matching $Ca_2Er_8Si_6O_{26}$ (ICDD #04-006-0315: hexagonal, rare-earth apatite) and $Ca_{0.37}Mg_{1.63}Al_4Si_5O_{18}$ (ICDD #04-002-2717: hexag-

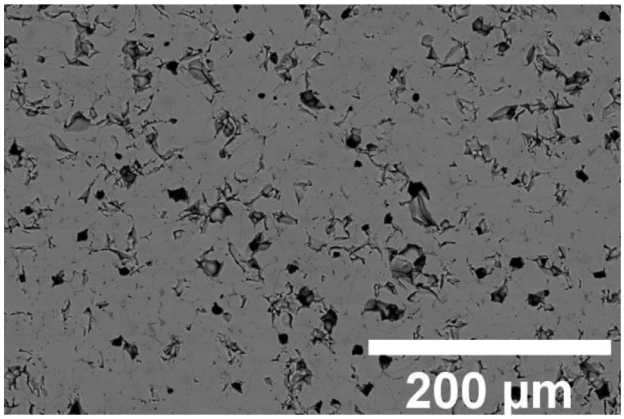

Fig. 5. Plan view SEM of bulk (ScNdErYbLu)MS after processing.

onal) were found after exposure, in agreement with the following energy dispersive spectroscopy (EDS) analysis. X-ray diffraction spectra of the EBC – CMAS reaction displayed clear texturing of the {100} hkl planes for the calcium-rare earth apatite reaction product, suggesting preferred growth directions for this reaction product phase. A logarithmic scale plot of the same data also presented a minor phase, $Ca_{0.37}Mg_{1.83}Al_{l4}Si_5O_{18}$, highlighting the crystallization of residual CMAS after exposure.

Higher magnification microscopy of the CMAS – (ScNdErYbLu)MS reaction interface is shown in Fig. 7. Residual glass remained on top of the sample surface, suggesting the reaction layer inhibited further glass penetration. Arrows adjacent to the figure indicated the reaction product layer formed between the glass and the sample. Residual CMAS contained multiple phases and compositional variance, as noted by the changes in greyscale. The base (ScNdErYbLu)MS material appeared uniformly mixed with only minor regions rich in Nd rare earth cation. Rare earths Nd, Er, Yb, and Lu were all present in the Ca-rich continuous reaction product, while Sc was primarily present in the residual CMAS. Dissolution of rare earths into the CMAS was observed by rare earth signal in the residual glass and by apatite phase precipitation within the residual glass. A Sc and Mg rich phase was also formed in the CMAS glass, due to a high concentration of Sc being dissolved compared to the other rare earth elements in solution.

Point EDS was performed five times and averaged on the dense apatite reaction phase at the interface and results are presented in Table 4. The Ca/RE signal ratio of 0.28 agreed with the ratio for apatite, $Ca_2RE_8Si_6O_{26}$ (Ca/RE = 0.25). Despite being an equimolar REMS, the rare earth cations were not evenly distributed within the apatite phase.

Table 4
Averaged point EDS of the dense apatite reaction layer between (ScNdErYbLu)MS and residual CMAS after thermal exposure to 1300 °C for 24 h.

Element	At. %	Element	At. %
O	40 ± 6	Nd	8 ± 1
Mg	0	Er	7.2 ± 0.8
Al	0	Yb	7.1 ± 0.8
Si	24 ± 2	Lu	5.4 ± 0.2
Ca	8 ± 1	Sc	0.8 ± 0.3

The concentration of rare earth elements in the apatite phase was seen to decrease with rare earth ionic radius, with Sc present only in trace quantities.

The rare earths Nd, Er, Yb, and Lu were present in the dense and continuous apatite reaction product at the EBC – CMAS interface. An average apatite reaction layer thickness was determined to be 47 ± 8 μm of the sample cross-section, compared to 48 ± 3 um for phase pure YbMS [17]. The amount of REMS dissolution, measured from the baseline sample height at unreacted sample edges to the apatite reaction layer, was 33 ± 8 μm, whereas phase pure YbMS was 58 ± 6 μm [17]. Negligible residual CMAS glass was apparent below the apatite layer, showing how (ScNdErYbLu)MS can act as a successful barrier to CMAS infiltration. (ScNdErYbLu)MS is expected to show further resistance to CMAS infiltration if highly dense material is tested, compared to the 89% dense material used in this work.

Larger rare earth elements preferentially formed the apatite phase at the CMAS – EBC interface. This trend has been shown for single rare earth apatites where rare earth cations with larger ionic radii have larger negative enthalpies of formation [20,21] and was inferred from work performed by Sun et al. for CMAS exposure of $(Er_{0.25}Tm_{0.25}Yb_{0.25}Lu_{0.25})$DS at 1500 °C [28]. The presence of a Mg and Sc rich crystalline phase in the residual glass suggested that the Sc-apatite phase was not stable. Additions of rare earth elements with larger ionic radii, such as Nd, into EBCs are thus expected to promote rapid formation of the apatite phase to limit total CMAS penetration.

3.3. Thermal expansion and thermal conductivity

The linear thermal expansion of both (ScNdErYbLu) phases are presented in Fig. 8 from 400 to 1250 °C. The CTEs of YbDS (measured via dilatometry as a part of this study), a SiC matrix [42], and silicon [43] were all fit to a linear equation for comparison. For reference, the average CTEs of the SiC matrix was 4.43 × 10^{-6}/°C from 400 to 1100 °C [42], and the average CTE of silicon was 4.26 × 10^{-6}/°C from 385 to 1150 °C [43]. (ScNdErYbLu)DS had an average linear CTE of 4.9 ± 0.4 × 10^{-6}/°C, which is an excellent CTE match to that of a SiC

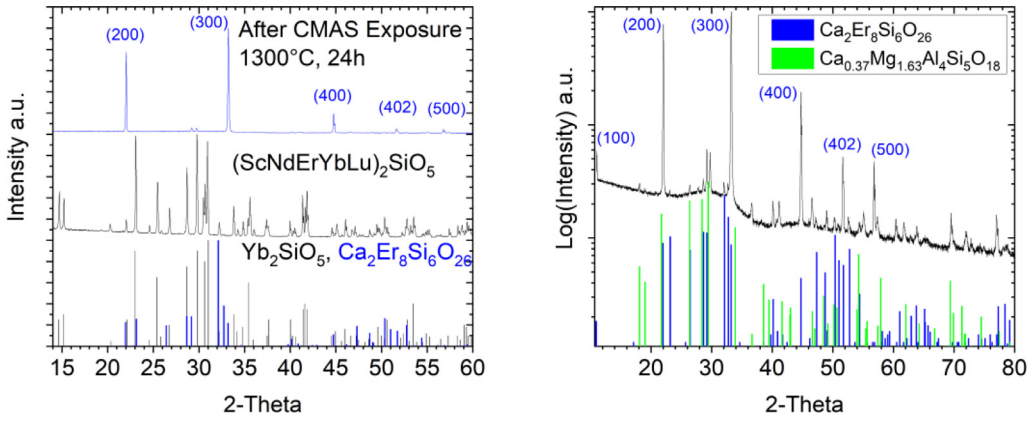

Fig. 6. XRD of (ScNdErYbLu)MS before and after CMAS exposure for 24 h at 1300 °C, in linear and logarithmic scale after CMAS exposure. The logarithmic scale plot of (ScNdErYbLu)MS after CMAS exposure shows a $Ca_{0.37}Mg_{1.63}Al_4Si_5O_{18}$ minor phase.

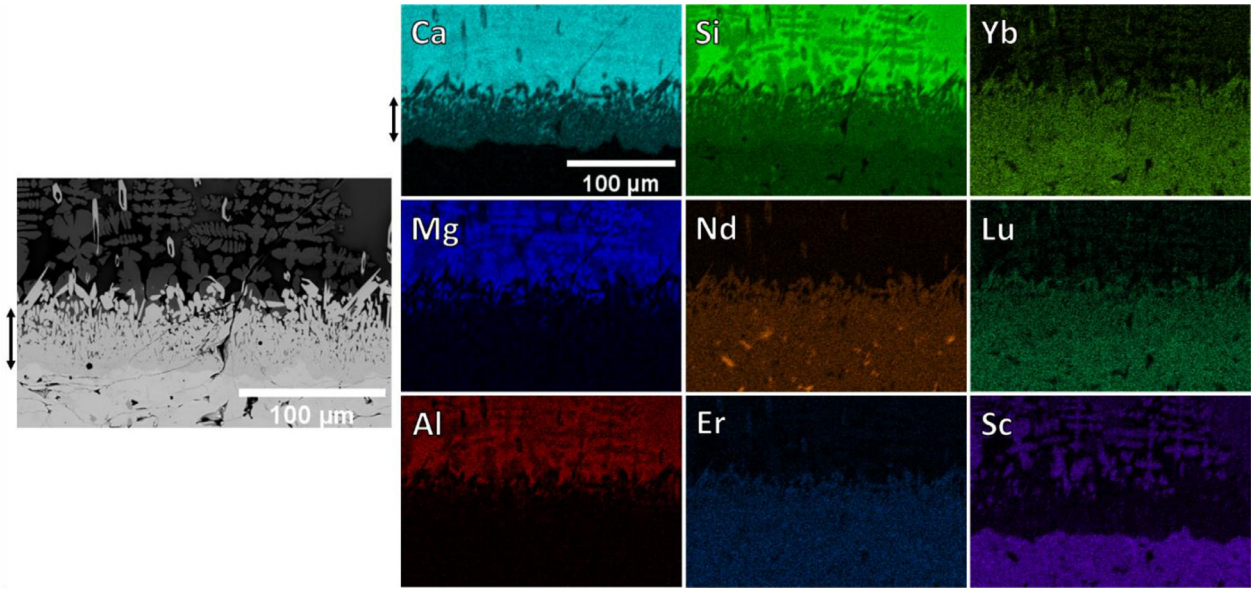

Fig. 7. Cross-section SEM of (ScNdErYbLu)MS after CMAS exposure for 24 h at 1300 °C with EDS mapping. Side arrows display the continuous reaction product layer that was present after CMAS exposure.

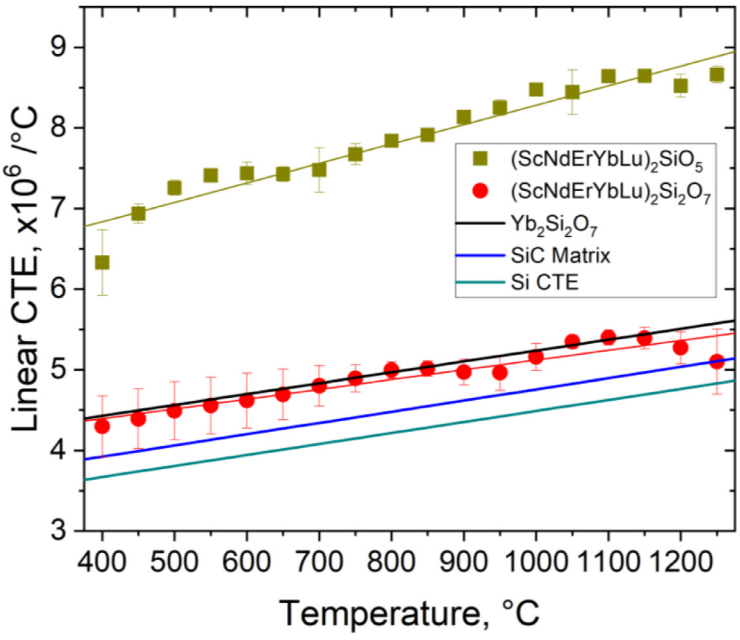

Fig. 8. Linear thermal expansion coefficients of (ScNdErYbLu) silicates, compared to linear fits for the CTEs of bulk YbDS (this work), a SiC matrix [42], and silicon [43].

matrix and silicon. A rule of mixtures (ROM) CTE for an equimolar (ScNdErYbLu)DS was calculated to be 4.85 × 10^{-6}/°C based on literature thermal expansion data for β-REDS (RE = Sc, Er, Yb, and Lu) and G-REDS (RE = Nd) [44]; also in agreement with the measured value obtained in this study. The additions of multiple rare earth elements did not distort the (ScNdErYbLu)DS thermal expansion far from that of YbDS. Bulk (ScNdErYbLu)MS had a linear CTE of 7.9 ± 0.8 × 10^{-6}/°C, which was in agreement with the rule of mixtures CTE of 7.74 × 10^{-6}/°C [22,45–48], yet too high of a value to be considered as a single layer EBC on SiC CMCs. Both (ScNdErYbLu) silicates maintained stable CTE values upon multiple temperature cycles, further signifying high-temperature phase stability discussed earlier with steam and CMAS exposures.

The room temperature thermal conductivities of both (ScNdErYbLu)DS and (ScNdErYbLu)MS were 2.61 ± 0.17 W/mK (W^{1}m^{-1} K^{-1}) and 1.08 ± 0.11 W/mK, respectively. These results were determined with TDTR, which included a measure of the average thermal boundary conductance at the interface of the Al metal transducer and multi-component barrier coating of interest; the measured thermal boundary conductance was 6.34 ± 3.44 × 10^7 MW/m^{2}K for (ScNdErYbLu)DS and 7.45 ± 3.88 × 10^7 MW/m^{2}K (ScNdErYbLu)MS across each sample. Room temperature thermal conductivities of YbDS and YbMS are 5.2 W/mK [30] and 2.2 W/mK [49], respectively. The thermal conductivity of both multi-component silicate systems was reduced by ~50% compared to the Yb silicates. The ~10 µm probe spot size used for TDTR was smaller than the Nd-rich REDS particles in the starting sample, which suggested that the thermal conductivity of the majority β-REDS phase dominated the value measured. The bulk thermal conductivity of (ScNdErYbLu)DS would likely be lower than 2.61 ± 0.17 W/mK due to the presence of porosity, grain boundaries, and phase boundaries in plasma sprayed EBCs, which are not expected to play a significant role in the present measurement technique due to the localized laser geometry used here.

4. Discussion

A holistic approach to design of multi-component rare earth silicates as next-generation EBC candidates was performed for the (ScNdErYbLu) silicate systems. Each rare earth cation contributed to EBC development through a variety of ways. Additions of Sc, Yb, and Lu all stabilized the desired low-CTE polymorphs for the rare earth silicates, such as β-phase REDS and X2-phase REMS. The presence of Er, Yb, and Lu helped stabilize the steam reaction product shown in Eq. (1). Apatite formation to minimize CMAS infiltration was promoted through addition of Nd with its larger ionic radius. It is possible that multicomponent rare earth silicates provide an increased stability of the apatite phase through site occupancy preferences dependent on rare earth bond strength, or rare earth ionic radius. The dual-phase (ScNdErYbLu)DS in this work did not show internal cracking or porosity changes upon annealing, steam exposure, or dilatometry measurements. As such, multi-component EBC materials may not be limited to single phase solid solution materials if all present phases do not display detrimental transformations within the temperature range of gas turbine engines.

Thermal expansion displayed only a minor dependence on rare earth cation based on an agreement with rule of mixtures CTEs. The major contributor to tailoring CTE was believed to be the crystal structure of the stabilized polymorph. Thus, multi-component REDS can be formulated with CTEs suitable for EBC materials if a low-CTE polymorph has been stabilized. Low thermal conductivities were present in both silicate phases through cation mass and ionic radius heterogeneity, attributed to increased phonon scattering and achieved by additions of Sc and Nd.

Utilizing the 16 available rare earth elements (including Sc and Y, excluding radioactive Pm), 4368 possible equimolar 5-component REDS compositions are available for tailoring thermal, chemical, and mechanical properties of rare earth silicate EBCs. EBC chemistries are also not limited to equimolar ratios; decreased Nd concentration in the current (ScNdErYbLu)DS is expected to decrease the presence of the secondary phase. Computational methods should utilize this wide compositional space to predict β-phase rare earth silicate mixtures that result in enhanced thermochemical and thermomechanical properties based on properties of individual rare earth silicate systems. Additional considerations should be used when searching for high-performance multi-component EBCs. First, the total cost of EBCs can be minimized through choosing rare earth additions that have relatively higher natural abundances. A general trend is present where larger ionic radii rare earth elements (such as Nd in this work) tend to be more abundant [50], with Y, Ce, and La representing the lowest cost material choices. As such, Y and larger ionic radii rare earth elements should be incorporated to some extent in the low-CTE β-REDS structure. Second, the impact of varied rare earth elements on the oxidation behavior of the silicon bond coat should be studied. Oxidation resistance can be determined via oxidation experiments of multi-component silicate EBCs or by oxygen tracer diffusion studies in bulk EBCs. Finally, the effect of the atmospheric plasma spray process (standard industrial EBC deposition method) on the phase stability of multi-rare earth silicate EBCs needs to be understood.

5. Conclusion

The present study on (ScNdErYbLu) silicate mixtures demonstrated the capability for T/EBC materials property optimization through introduction and stabilization of multiple rare earth cations into preferred EBC phases. RE = Er, Yb, and Lu supported steam resistance, RE = Nd enhanced CMAS resistance, RE = Sc and Nd decreased thermal conductivity, and RE = Sc, Yb, and Lu promoted phase stability. (ScNdErYbLu)DS was exposed to high-velocity steam at 1400 °C for 125 h, producing a porous and single phase (ScNdErYbLu)MS reaction product on the sample surface that was both more thermochemically stable and more robust than the YbMS formed on YbDS alone. A bulk (ScNdErYbLu)MS sample was then exposed to CMAS at 1300 °C for 24 h to model the interaction between an EBC – steam reaction product and molten CMAS. A continuous and dense interfacial apatite reaction product formed that limited further CMAS ingress into the bulk sample, with preferred incorporation of rare earth elements with larger ionic radii. The CTE of (ScNdErYbLu)DS remained in an acceptable range for application on SiC CMCs. Thermal conductivity of the multicomponent rare earth silicates was reduced by ~50% relative to the individual ytterbium silicate constituents. Multi-component rare earth silicates thus enable dual-purpose T/EBC materials with tailored thermal, chemical, and mechanical properties.

Declaration of Competing Interest

The authors declare that they have no known competing financial interests or personal relationships that could have appeared to influence the work reported in this paper.

Acknowledgments

This work was funded through the National Science Foundation DMREF: Collaborative Research: GOALI: Accelerating Discovery of High Entropy Silicates for Extreme Environments, Award #1921973. We also appreciate support from the Office of Naval Research, Grant No. N00014-21-1-2477. The authors would like to acknowledge the Nanoscale Materials Characterization Facility at the University of Virginia for supporting this research through characterization equipment.

Supplementary materials

Supplementary material associated with this article can be found, in the online version, at doi:10.1016/j.mtla.2022.101557.

References

[1] M.J. Walock, V. Heng, A. Nieto, A. Ghoshal, M. Murugan, D. Driemeyer, Ceramic matrix composite materials for engine exhaust systems on next-generation vertical lift vehicles, J. Eng. Gas Turbines Power 140 (102101) (2018), doi:10.1115/1.4040011.
[2] T.H. Nguyen, P.T. Nguyen, F. Garnier, Evaluation of the relationship between the aerothermodynamic process and operational parameters in the high-pressure turbine of an aircraft engine, Aerosp. Sci. Technol. 86 (2019) 93–105, doi:10.1016/j.ast.2019.01.011.
[3] M.K. Ferber, H.T. Lin, Environmental characterization of monolithic ceramics for gas turbine applications, Key Eng. Mater. 287 (2005) 367–380, doi:10.4028/www.scientific.net/KEM.287.367.
[4] E.J. Opila, R.E. Hann, Paralinear oxidation of CVD SiC in water vapor, J. Am. Ceram. Soc. 80 (1) (1997) 197–205, doi:10.1111/j.1151-2916.1997.tb02810.x.
[5] E.J. Opila, Oxidation and volatilization of silica formers in water vapor, J. Am. Ceram. Soc. 86 (8) (2003) 1238–1248, doi:10.1111/j.1151-2916.2003.tb03459.x.
[6] M.J. Ridley, E.J. Opila, Variable thermochemical stability of $RE_2Si_2O_7$ (RE = Sc, Nd, Er, Yb, or Lu) in high-temperature high-velocity steam, J. Am. Ceram. Soc. (2021), doi:10.1111/jace.18120.
[7] S. Ueno, D.D. Jayaseelan, H. Kita, T. Ohji, H.T. Lin, Comparison of water vapor corrosion behaviors of $Ln_2Si_2O_7$ (Ln=Yb and Lu) and $ASiO_4$ (A=Ti, Zr and Hf) EBC's, Key Eng. Mater. 317–318 (2006) 557–560, doi:10.4028/www.scientific.net/KEM.317-318.557.
[8] H. Klemm, Silicon nitride for high-temperature applications, J. Am. Ceram. Soc. 93 (6) (2010) 1501–1522, doi:10.1111/j.1551-2916.2010.03839.x.
[9] M. Ridley, E. Opila, Thermochemical stability and microstructural evolution of $Yb_2Si_2O_7$ in high-velocity high-temperature water vapor, J. Eur. Ceram. Soc. 41 (5) (2020) 3141–3149, doi:10.1016/j.jeurceramsoc.2020.05.071.
[10] B.T. Richards, K.A. Young, F. de Francqueville, S. Sehr, M.R. Begley, H.N.G. Wadley, Response of ytterbium disilicate–silicon environmental barrier coatings to thermal cycling in water vapor, Acta Mater. 106 (Supplement C) (Mar. 2016) 1–14, doi:10.1016/j.actamat.2015.12.053.
[11] R.I. Webster, E.J. Opila, Viscosity of CaO-MgO-Al_2O_3-SiO_2 (CMAS) melts: Experimental measurements and comparison to model calculations, J. Non Cryst. Solids 584 (2022) 121508, doi:10.1016/j.jnoncrysol.2022.121508.
[12] K.M. Grant, S. Krämer, J.P.A. Löfvander, C.G. Levi, CMAS degradation of environmental barrier coatings, Surf. Coat. Technol. 202 (4) (2007) 653–657, doi:10.1016/j.surfcoat.2007.06.045.
[13] F. Stolzenburg, M.T. Johnson, K.N. Lee, N.S. Jacobson, K.T. Faber, The interaction of calcium–magnesium–aluminosilicate with ytterbium silicate environmental barrier materials, Surf. Coat. Technol. 284 (2015) 44–50, doi:10.1016/j.surfcoat.2015.08.069.
[14] V.L. Wiesner, B.J. Harder, N.P. Bansal, High-temperature interactions of desert sand CMAS glass with yttrium disilicate environmental barrier coating material, Ceram. Int. 44 (18) (2018) 22738–22743, doi:10.1016/j.ceramint.2018.09.058.

[15] L.R. Turcer, A.R. Krause, H.F. Garces, L. Zhang, N.P. Padture, Environmental-barrier coating ceramics for resistance against attack by molten calcia-magnesia-aluminosilicate (CMAS) glass: part I, $YAlO_3$ and γ-$Y_2Si_2O_7$, J. Eur. Ceram. Soc. 38 (11) (2018) 3905–3913, doi:10.1016/j.jeurceramsoc.2018.03.021.

[16] L.R. Turcer, A.R. Krause, H.F. Garces, L. Zhang, N.P. Padture, Environmental-barrier coating ceramics for resistance against attack by molten calcia-magnesia-aluminosilicate (CMAS) glass: Part II, β-$Yb_2Si_2O_7$ and β-$Sc_2Si_2O_7$, J. Eur. Ceram. Soc. 38 (11) (2018) 3914–3924, doi:10.1016/j.jeurceramsoc.2018.03.010.

[17] R.I. Webster, E.J. Opila, Mixed phase ytterbium silicate environmental-barrier coating materials for improved calcium–magnesium–alumino-silicate resistance, J. Mater. Res. 35 (17) (2020) 2358–2372, doi:10.1557/jmr.2020.151.

[18] J. Felsche, Rare earth silicates with the apatite structure, J. Solid State Chem. 5 (2) (1972) 266–275, doi:10.1016/0022-4596(72)90039-4.

[19] L.R. Turcer, N.P. Padture, Rare-earth pyrosilicate solid-solution environmental-barrier coating ceramics for resistance against attack by molten calcia–magnesia–aluminosilicate (CMAS) glass, J. Mater. Res. 35 (17) (2020) 2373–2384, doi:10.1557/jmr.2020.132.

[20] G. Costa, B.J. Harder, N.P. Bansal, B.A. Kowalski, J.L. Stokes, Thermochemistry of calcium rare-earth silicate oxyapatites, J. Am. Ceram. Soc. 103 (2) (2020) 1446–1453, doi:10.1111/jace.16816.

[21] A.S. Risbud, K.B. Helean, M.C. Wilding, P. Lu, A. Navrotsky, Enthalpies of formation of lanthanide oxyapatite phases, J. Mater. Res. 16 (10) (2001) 2780–2783, doi:10.1557/JMR.2001.0381.

[22] L.R. Turcer, N.P. Padture, Towards multifunctional thermal environmental barrier coatings (TEBCs) based on rare-earth pyrosilicate solid-solution ceramics, Scr. Mater. 154 (2018) 111–117, doi:10.1016/j.scriptamat.2018.05.032.

[23] J. Felsche, The Crystal Chemistry of the Rare-Earth Silicates, in rare earths, Springer, 1973, pp. 99–197.

[24] A.J. Fernández-Carrión, M.D. Alba, A. Escudero, A.I. Becerro, Solid solubility of $Yb_2Si_2O_7$ in β-, γ- and δ-$Y_2Si_2O_7$, J. of Solid State Chem. 184 (7) (2011) 1882–1889, doi:10.1016/j.jssc.2011.05.034.

[25] P.I. Stack, K.A. Kane, M. Sweet, C.G. Parker, M.J. Lance, M.J. Ridley, B.A. Pint, Dry air cyclic oxidation of mixed Y/Yb disilicate environmental barrier coatings and bare silica formers, J. Eur. Ceram. Soc. 42 (7) (2022) 3345–3350, doi:10.1016/j.jeurceramsoc.2022.02.009.

[26] M.J. Ridley, K.A. Kane, M.J. Lance, C.G. Parker, Y.F. Su, S. Sampath, E. Garcia, M. Sweet, M. O'Connor, B.A. Pint, Steam oxidation and microstructural evolution of rare earth silicate environmental barrier coatings, J. Am. Ceram. Soc. (2022), doi:10.1111/jace.18769.

[27] Y. Dong, K. Ren, Y. Lu, Q. Wang, J. Liu, Y. Wang, High-entropy environmental barrier coating for the ceramic matrix composites, J. Eur. Ceram. Soc. 39 (7) (2019) 2574–2579, doi:10.1016/j.jeurceramsoc.2019.02.022.

[28] L. Sun, et al., High temperature corrosion of $(Er_{0.25}Tm_{0.25}Yb_{0.25}Lu_{0.25})_2Si_2O_7$ environmental barrier coating material subjected to water vapor and molten calcium–magnesium–aluminosilicate (CMAS), Corros. Sci. 175 (2020) 108881, doi:10.1016/j.corsci.2020.108881.

[29] M.J. Ridley, J. Gaskins, P. Hopkins, E.J. Opila, Tailoring thermal properties of multi-component rare earth monosilicates, Acta Mater. 195 (2020) 698–707, doi:10.1016/j.actamat.2020.06.012.

[30] L.R. Turcer, A. Sengupta, N.P. Padture, Low thermal conductivity in high-entropy rare-earth pyrosilicate solid-solutions for thermal environmental barrier coatings, Scr. Mater. 191 (2021) 40–45, doi:10.1016/j.scriptamat.2020.09.008.

[31] Y. Sun, H. Xiang, F. Dai, X. Wang, Y. Xing, X. Zhao, Y. Zhou, Preparation and properties of CMAS resistant bixbyite structured high-entropy oxides RE_2O_3 (RE = Sm, Eu, Er, Lu, Y, and Yb): promising environmental barrier coating materials for Al_2O_3f/Al_2O_3 composites, J. Adv. Ceram. 10 (2021) 596–613, doi:10.1007/s40145-021-0461-6.

[32] J. Zhu, X. Meng, J. Xu, P. Zhang, Z. Lou, M. Reece, F. Gao, Ultra-low thermal conductivity and enhanced mechanical properties of high-entropy rare earth niobates (RE_3NbO_7, RE = Dy, Y, Ho, Er, Yb), J. Eur. Ceram. Soc. 41 (1) (2021) 1052–1057, doi:10.1016/j.jeurceramsoc.2020.08.070.

[33] R.A. Golden, E.J. Opila, A method for assessing the volatility of oxides in high-temperature high-velocity water vapor, J. Eur. Ceram. Soc. 36 (5) (2016) 1135–1147, doi:10.1016/j.jeurceramsoc.2015.11.016.

[34] S.L. dos Santos e Lucato, O.H. Sudre, D.B. Marshall, A method for assessing reactions of water vapor with materials in high-speed, high-temperature flow, J. Am. Ceram. Soc. 94 (2011) s186–s195, doi:10.1111/j.1551-2916.2011.04556.x.

[35] C.G. Parker, E.J. Opila, Stability of the Y_2O_3-SiO_2 system in high-temperature, high-velocity water vapor, J. Am. Ceram. Soc. (2019) 16915, doi:10.1111/jace.16915.

[36] R. Golden, Matrix Development for Water Vapor Resistant SiC-Based Ceramic Matrix Composites, University of Virginia, 2017, doi:10.18130/V3B34Z.

[37] D.L. Poerschke, G.G.E. Seward, C.G. Levi, Influence of Yb:Hf Ratio on ytterbium hafnate/molten silicate (CMAS) reactivity, J. Am. Ceram. Soc. 99 (2) (2016) 651–659, doi:10.1111/jace.13964.

[38] J.L. Braun, D.H. Olson, J.T. Gaskins, P.E. Hopkins, A steady-state thermoreflectance method to measure thermal conductivity, Rev. Sci. Instrum. 90 (2) (2019) 024905, doi:10.1063/1.5056182.

[39] D.H. Olson, J.L. Braun, P.E. Hopkins, Spatially resolved thermoreflectance techniques for thermal conductivity measurements from the nanoscale to the mesoscale, J. Appl. Phys. 126 (15) (2019) 150901, doi:10.1063/1.5120310.

[40] P. Jiang, X. Qian, R. Yang, Tutorial: time-domain thermoreflectance (TDTR) for thermal property characterization of bulk and thin film materials, J. Appl. Phys. 124 (16) (2018) 161103, doi:10.1063/1.5046944.

[41] D.G. Cahill, Analysis of heat flow in layered structures for time-domain thermoreflectance, Rev. Sci. Instrum. 75 (12) (2004) 5119–5122, doi:10.1063/1.1819431.

[42] X. Fan, X. Ma, X. Dang, J. Xue, F. Ye, D. Zhao, L. Cheng, In-plane thermal expansion behavior of dense ceramic matrix composites containing SiBC matrix, J. Eur. Ceram. Soc. 40 (9) (2020) 3414–3422, doi:10.1016/j.jeurceramsoc.2020.03.006.

[43] Y. Okada, Y. Tokumaru, Precise determination of lattice parameter and thermal expansion coefficient of silicon between 300 and 1500 K, J. Appl. Phys. 56 (2) (1984) 314–320, doi:10.1063/1.333965.

[44] A.J. Fernández-Carrión, M. Allix, A.I. Becerro, Thermal expansion of rare-earth pyrosilicates, J. Am. Ceram. Soc. 96 (7) (2013) 2298–2305, doi:10.1111/jace.12388.

[45] N. Al Nasiri, N. Patra, D. Horlait, D.D. Jayaseelan, W.E. Lee, Thermal properties of rare-earth monosilicates for EBC on Si-based ceramic composites, J. Am. Ceram. Soc. 99 (2) (2016) 589–596, doi:10.1111/jace.13982.

[46] Z.S. Khan, B. Zou, W. Huang, X. Fan, L. Gu, X. Chen, S. Zeng, C. Wang, X. Cao, Synthesis and characterization of Yb and Er based monosilicate powders and durability of plasma sprayed Yb_2SiO_5 coatings on C/C–SiC composites, Mater. Sci. Eng. B 177 (2) (2012) 184–189, doi:10.1016/j.mseb.2011.12.004.

[47] D. Zhu, L. Kang, Thermal expansion and thermal conductivity of rare earth silicates, in: Proceedings of the International Conference on Advanced Ceramics and Composites„ 2006 Accessed: Jan. 08, 2018. [Online]. Available:.

[48] S. Ramasamy, S.N. Tewari, K.N. Lee, R.T. Bhatt, D.S. Fox, EBC development for hot-pressed Y_2O_3/Al_2O_3 doped silicon nitride ceramics, Mater. Sci. Eng. A 527 (21–22) (2010) 5492–5498, doi:10.1016/j.msea.2010.05.067.

[49] Z. Tian, L. Zheng, J. Wang, P. Wan, J. Li, J. Wang, Theoretical and experimental determination of the major thermo-mechanical properties of RE_2SiO_5 (RE=Tb, Dy, Ho, Er, Tm, Yb, Lu, and Y) for environmental and thermal barrier coating applications, J. Eur. Ceram. Soc. 36 (1) (2016) 189–202, doi:10.1016/j.jeurceramsoc.2015.09.013.

[50] K.H. Wedepohl, The composition of the continental crust, Geochim. et Cosmochim. Acta 59 (7) (1995) 1217–1232, doi:10.1016/0016-7037(95)00038-2.